Article

Reflectance in AFM-IR: Implications for Interpretation and Remote Analysis of the Buried Interface

Suzanne Morsch,* Stuart Lyon, Steve Edmondson, and Simon Gibbon
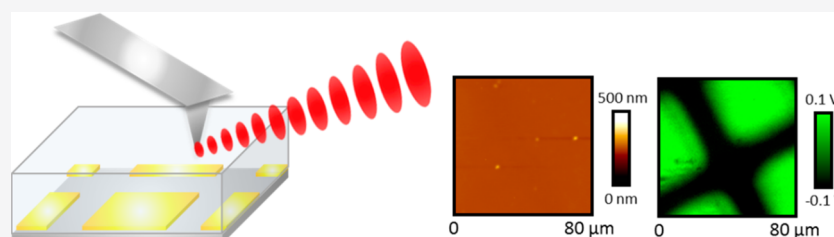
Read Online

ACCESS | Metrics & More | Article Recommendations | Supporting Information

ABSTRACT: AFM-IR combines the chemical sensitivity of infrared spectroscopy with the lateral resolution of scanning probe microscopy, allowing nanoscale chemical analysis of almost any organic material under ambient conditions. As a result, this versatile technique is rapidly gaining popularity among materials scientists. Here, we report a previously overlooked source of data and artifacts in AFM-IR analysis; reflection from the buried interface. Periodic arrays of gold on glass are used to show that the overall signal in AFM-IR is affected by the wavelength-dependent reflectivity and thermal response of the underlying substrate. Excitingly, this demonstrates that remote analysis of heterogeneities at the buried interface is possible alongside that of an overlying organic film. On the other hand, AFM-IR users should carefully consider the composition and topography of underlying substrates when interpreting nanoscale infrared data. The common practice of generating ratio images, or indeed the normalization of AFM-IR spectra, should be approached with caution in the presence of substrate heterogeneity or variable sample thickness.

In recent decades, innovative techniques combining atomic force microscopy (AFM) with vibrational spectroscopy have opened up a new frontier in materials analysis, producing chemical maps with resolutions which far surpass the Rayleigh diffraction limit, in the range of 10−100 nm.[1,2] This rapidly developing field encompasses tip-enhanced Raman spectroscopy (TERS),[3] scattering scanning nearfield optical microscopy (s-SNOM),[4] and photothermal infrared techniques (AFM-IR).[5] Of these, the photothermal AFM-IR approach has quickly gained popularity among material scientists due to its simplicity and versatility.[6]

During AFM-IR, the diffraction-limit associated with conventional microspectroscopy optics is side-stepped by monitoring the thermal expansion of materials induced by the absorption of infrared radiation, using an AFM probe in contact with the sample surface as the detector, Scheme 1. In contrast to s-SNOM, this approach gives a direct measure of infrared absorption, simplifying interpretation. In addition, AFM-IR does not require rigorously defined probe tip geometries and is less sensitive to contamination than TERS. As a result, since its inception, the AFM-IR approach has been applied to an ever expanding range of specimens spanning materials science disciplines. Recent examples include the identification of local degradation processes in organic coatings,[7,8] fibers,[9] oil paint[10] and solid state insulators,[11] minerals in bitumen,[12] geological specimens,[13,14] bone[15] and

Scheme 1. AFM-IR Experimental Set up with Pulsed Ir Illumination via (a) a Bottom-up Configuration Through a ZnSe Prism and (b) with Top-down Illumination
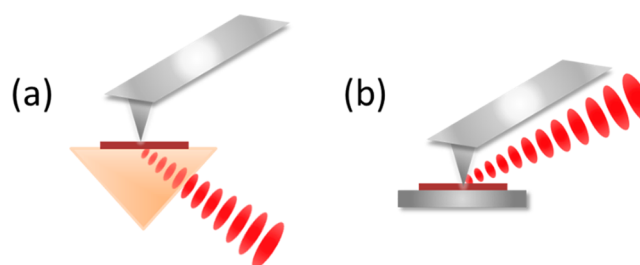
human dentin,[16] the analysis of corrosion inhibitor films,[17] individual aerosol particles,[18,19] nanoscale domains found in polymer blends,[20−23] thermosets[24−26] and nanocomposites,[27] the chemical groups on 2D nanomaterials,[28,29] and new

insights into protein folding,[30,31] subcellular structures,[32] and plant epicutular wax.[33]

A significant factor contributing to the recent widespread application of AFM-IR has been the introduction and commercialization of a top-down illumination setup,[34] which has allowed a range of samples supported by any underlying substrate to be analyzed. In contrast, the original bottom-up illumination experiment necessitated the preparation of thin specimens in good contact with a ZnSe prism,[35−38] Scheme 1. The top-down configuration has allowed specimen geometries to become less restricted and, hence, the adoption of AFM-IR as a routine analysis technique. However, one important consequence of this is the need to understand and eliminate potential infrared imaging artifacts.[2,39] For AFM-IR, previously reported sources of artifact in the infrared signal include variation in the tip−sample contact area on rough samples,[11] locally enhanced infrared amplitude signals over regions of increased sample thickness (i.e., increased volume of material beneath the probe),[39,40] and the dependence of the induced resonance on local mechanical properties (hardness).[41,42] At present, these effects are, for the most part, routinely considered by experienced microscopists when interpreting AFM-IR results. Since the aforementioned phenomena are all wavelength-independent, these can often be ruled out or eliminated by the examination of normalized local spectra and by the production of ratio maps (where infrared maps taken at two different wavenumbers are divided, in a process akin to spectral normalization). Here we report a new source of artifact and information which has previously gone unnoticed. Namely, features dependent on reflection of the incident infrared from an underlying substrate can appear in AFM-IR infrared spectra and maps. More importantly, since this effect is wavelength-dependent, it would not be corrected for by normalization approaches.

■ EXPERIMENTAL SECTION

Sample Preparation. 0.5−10% w/w solutions of polystyrene (Sigma-Aldrich, analytical standard, average M_w = 290,000) in toluene (Fisher Scientific, >99%) were cast (Oscilla spin coater, spin speeds 1000−6000 rpm) onto gold decorated glass substrates, in order to generate layers of varying thickness. Periodic arrays of gold were prepared by depositing gold (Quorum150R Rotary-Pumped Sputter Coater) onto borosilicate glass microscope slides (VWR) through a 400 mesh TEM grid. Gold thickness was assessed by AFM profile analysis across scratched regions, using Peakforce Tapping mode images obtained on a Bruker Mulitmode 8. Polystyrene film thicknesses were assessed directly using either laser microscopy (Keyence X200 K 3D Laser microscope) or AFM profile analysis (Bruker NanoIR2) across a scratched region of the coating by determining the step edge height.

FTIR (Fourier Transform Infrared) Spectroscopy. Reflectance FTIR spectra of samples were obtained using a FTIR-spectrometer (Nicolet 5700 spectrometer, Thermo Electron Corp.) equipped with room-temperature DTGS (deuterated triglycine sulfate) detector operating at 4 cm^{-1} resolution across the 4000−500 cm^{-1} range. Sixty-four co-averages were added to every spectrum.

Atomic Force Microscopy-Infrared Analysis (AFM-IR). Nanoscale infrared analysis was performed on a NanoIR2 system (Bruker) operating with top-down illumination. During AFM-IR, the sample is subjected to rapid pulses (10 ns duration at a repetition rate of 1 kHz) from a tunable infrared

source (optical parametric oscillators, approximate beam spot size 30 μm, power 1−10 mW across the spectral range). Absorption of infrared radiation induces abrupt thermal expansion of the sample, and this is detected by deflection of an AFM probe in contact with the surface. The recorded AFM-IR signal then corresponds to the amplitude of induced oscillation after fast Fourier transform. It has repeatedly been shown that for polymers plotting this signal as a function of IR wavelength yields spectra closely matched to those obtained by macroscopic FTIR.[15,40,43,44] Furthermore, since the IR pulse (10 ns duration), thermal expansion, and damping down of the induced oscillation occur on a faster time scale than the feedback electronics of the AFM, simultaneous contact-mode topographical measurement and IR absorption mapping can be performed at a given wavelength.[8,45−47] For the present study, AFM-IR images were collected in a contact mode at a scan rate of 0.04 Hz using a gold-coated silicon nitride probe (0.07−0.4 N/m spring constant, 13 ± 4 kHz resonant frequency, Bruker). Maps were obtained using 32 co-averages for 600 points per 300 scan lines. Spectra were obtained using 1024 co-averages for each data point. Background spectra were used to correct for atmospheric IR absorption and laser power fluctuations. These were subtracted automatically by the software and were collected once per day, using 5 averaged spectra with 1024 co-averages for each data point across the spectral range.

The angle of refraction of the infrared through the polystyrene films was calculated to be 33.2° with respect to the normal by Snell's Law, using the literature value of 1.58 for the refractive index of polystyrene in the mid-infrared region[48] and the manufacturer-supplied incident angle of 60 degrees from the normal. These values are subsequently used to estimate the path length through polystyrene films of variable thickness and reflectivity of the air−polymer interface using the Fresnel equations.

■ RESULTS

Reflectance Effects in AFM-IR Maps and Spectra. To investigate the effect of reflectance on AFM-IR analysis, model substrates with locally contrasting reflectivity were constructed by sputtering gold onto borosilicate glass through TEM (transmission electron microscopy) grids. This simple micro-patterning technique was verified using scanning electron microscopy, where backscattered electron images and EDS (energy-dispersive X-ray spectroscopy) elemental maps confirmed the selective deposition of a periodic gold array, Figure 1a−c.

High-resolution peakforce tapping mode AFM (atomic force microscopy) was performed on the patterned regions before and after coating with polystyrene. Height images revealed that the deposited gold was nodular in structure, with a measured thickness of 27 nm ±4 nm and Ra values of 0.36 nm, Figure 1d. Polystyrene was then cast from solution onto the gold-decorated glass. After coating, the nanoscale morphology of cast polystyrene layers was found to be more homogeneous than the underlying gold (Ra value of 0.15 nm), demonstrating complete coverage of the underlying patterned substrate, Figure 1e. The thickness of deposited polymer layers was varied from 90 to 3000 nm by altering both the solution viscosity (1−10% w/w in toluene) and spin coating speed (1000−6000 rpm).

Next, AFM-IR analysis was performed for the polystyrene films. Figure 2 shows the local spectra and maps gathered for a 1200 nm thick layer of polystyrene, where the infrared
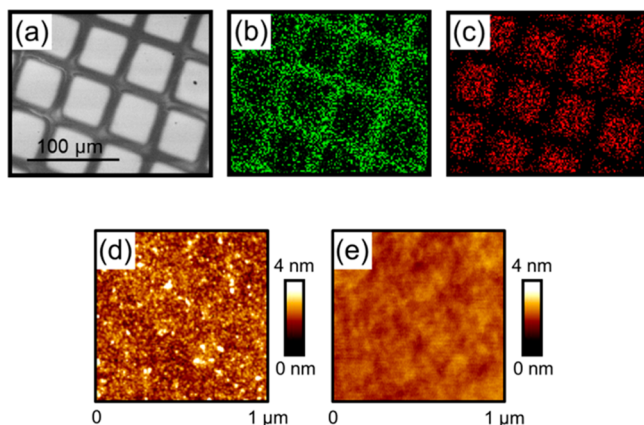
Figure 1. Microscopy images of a periodic gold on glass substrate prepared by sputtering gold through a 400 mesh TEM grid onto borosilicate glass: (a) backscattered SEM image alongside the corresponding (b) oxygen EDS map and (c) gold EDS map; high resolution peak force tapping mode AFM image of the sputtered gold region (d) before and (e) after spin-casting of a 1200 nm thick polystyrene film.

Figure 3. FTIR reflectance-mode spectra of borosilicate glass, and borosilicate glass with 7, 31, and 82 nm thick sputter-coated gold layers.

amplitude maps clearly show an enhanced signal over the underlying gold-coated squares, although the contrast was found to be dependent on the incident wavelength. This was found to be the case for all the thin films tested, and this wavelength-dependency was further confirmed by comparison to the local spectra.

Conventional reflectance mode FTIR spectroscopy showed that for the thicknesses of gold deposited onto patterned substrates (27 ± 4 nm), the gold coated regions should be substantially more reflective than borosilicate glass across the entire mid-IR range (although absolute reflectivity values will of course differ due to the difference between the incident angle achieved in air and polystyrene, and the difference in refractive index), Figure 3. Nonetheless, the relatively higher reflectivity of gold explains the enhanced AFM-IR signal, since the infrared reflecting off the gold substrate passes twice through the polymer film, producing a bigger photothermal response. Over glass, for most wavelengths the infrared is transmitted through the substrate, escaping the sample having only passed through the polymer film once (to a first
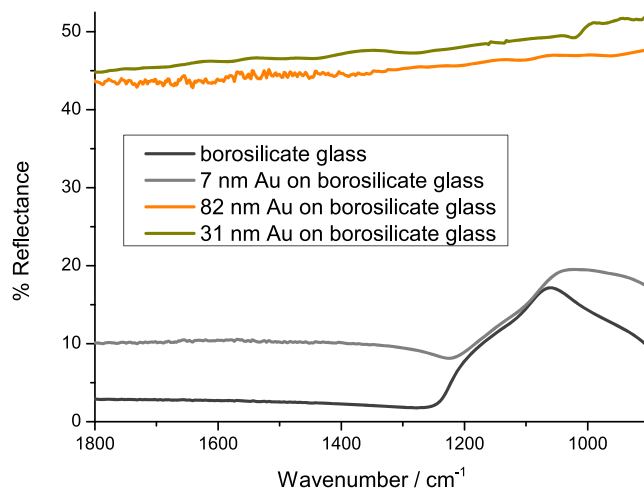
approximation, see Figure S1 for a detailed treatment of reflected intensities).

Furthermore, for borosilicate glass, a broad infrared reflectance band is clearly observed at 1076 cm^{-1}, corresponding to the band observed in AFM-IR spectra over glass regions. This is attributed to asymmetric Si−O−Si bond stretching.[49] In the case of AFM-IR spectra, polystyrene is also known to have several weak bands in this range, which are overlaid on the large SiO$_2$ peak, giving it a more complex shape. Overall the glass spectra correspond well to the reported variations in the complex refractive index of silicate and borosilicate glasses across the infrared region[50,51] and to our calculations of the reflectivity increase expected at this wavelength (e.g., 4% reflectivity at 1600 cm^{-1}, 53% reflectivity at 1076 cm^{-1}, see Table S1).

The above analysis of FTIR spectra supports the hypothesis that AFM-IR amplitude signals correspond to the reflectivity of the underlying substrate, i.e., reflectance of the infrared back into the film results in increased absorption by the polystyrene. However, a more detailed consideration of reflectivity is required to explain the lower contrast obtained in infrared
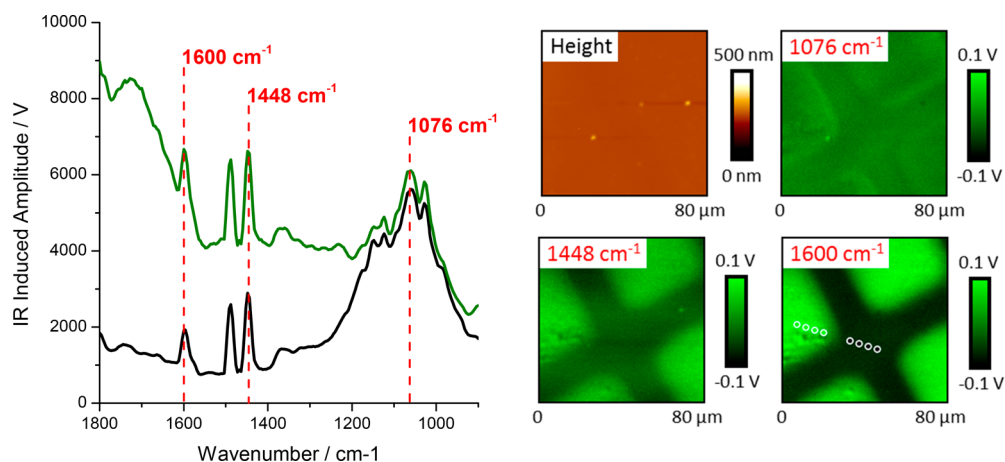

Figure 2. (Left) AFM-IR spectra of 1200 nm thick polystyrene on the gold sputtered region (green) and on the glass (black). (Right) AFM-IR contact mode height image and corresponding infrared maps gathered at 1076, 1448, and 1600 cm^{-1}. Spectra correspond to the average obtained for four individual measurements at the locations indicated by markers.
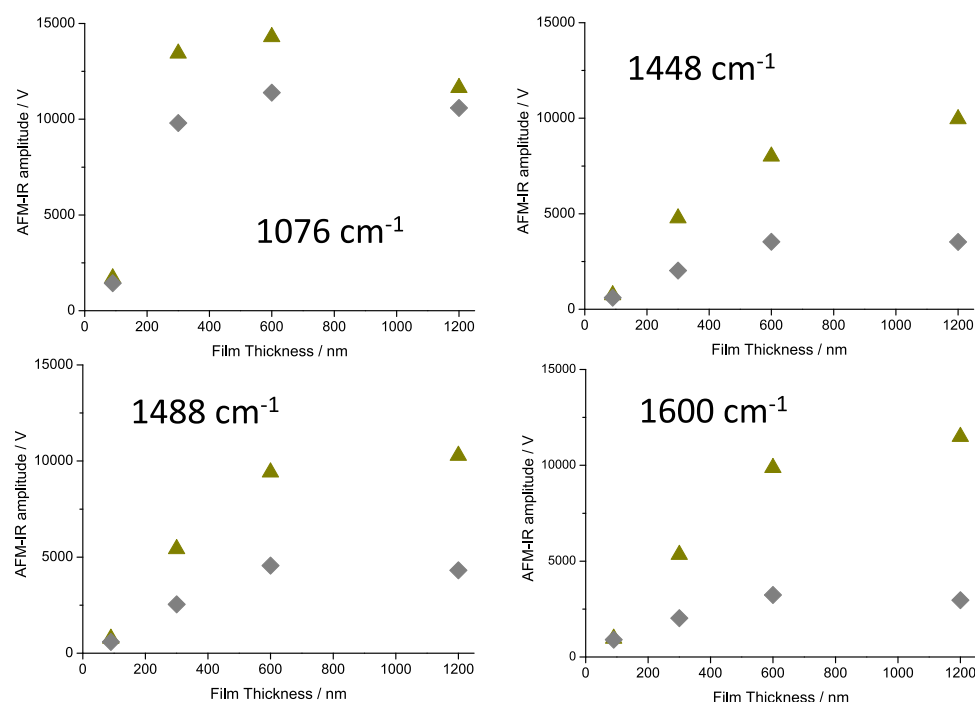
Figure 4. AFM-IR amplitude values obtained from the average of four individual spectra collected over gold (yellow ▲) and glass (gray ◆) regions at 1076, 1448, 1488, and 1600 cm^{-1}, as a function of the overlying polystyrene film thickness.

maps at 1076 cm^{-1}, corresponding to the Si–O–Si bond. As the glass/polystyrene interface becomes partially reflective at this wavelength (41% calculated reflectivity, Table S1), the intensity over glass will be enhanced by a partial second pass of the infrared though the polymer film (see Figure S3). Furthermore, since significant infrared is also entering the glass substrate at a wavelength at which it now strongly adsorbs, we must also consider the photothermal detection technique operational during AFM-IR analysis. Although the glass will be heated from infrared adsorption, this contribution may be small given the much lower coefficient of thermal expansion compared to polymer and the remoteness from the detecting tip. However, the thermal response of the underlying substrate could be amplified by thermal expansion of the overlying organic film, similar to an effect recently shown for AFM-IR of graphene on polymer substrates.[52]

In order to investigate this, detailed analysis of the AFM-IR amplitude signals was performed for polystyrene films of variable thickness. To a first approximation, the AFM-IR amplitude signal of organic specimens has been shown to be directly proportional to infrared absorption,[45] and, for a given polymer, since infrared absorption follows the Beer–Lambert law, this should scale with the effective path length, i.e., film thickness. Indeed, correlation between the local sample thickness and AFM-IR amplitude signal has previously been demonstrated to exist for polystyrene beads of < 750 nm thickness.[53] In the present case, the AFM-IR amplitude signal was assessed using the average spectrum generated from four individual readings over both the gold-coated glass and glass regions, as shown in Figure 2 for 1200 nm thick polystyrene. The results for polystyrene layers of 90, 300, and 600 nm thickness demonstrate that the raw AFM-IR infrared-induced amplitude signal signals do indeed scale linearly for submicron film thicknesses, and this is found to be the case over both

gold-decorated glass and glass regions for signals at 1448, 1488, and 1600 cm^{-1}, Figure 4. For the 1200 nm thick films, however, this correlation breaks down, which we propose is likely due to a nonlinear response of the AFM-IR to intense absorptions as the detection mechanism becomes saturated.

When considering reflection, enhancement of the infrared amplitude signal should also increase as a function of the film thickness (again corresponding to the increased path length). Thus, evidence for the reflection effect can be found in the increasing difference between the AFM-IR amplitude signal over gold and glass regions (corresponding to the increase caused by reflection only) at 1448, 1488, and 1600 cm^{-1}, although these increases are not linear, Figure 5. This interpretation is also supported by the full optical modeling at 1600 cm^{-1} given in Figure S2, with the difference in absorption between gold and glass increasing (although not linearly and slightly nonmonotonically) between 90 and 1200 nm thickness. We note that the spectrum over gold in Figure 2 has an unexplained baseline amplitude increase from 1600 to 1800 cm^{-1}. For this reason, no detailed interpretation has been attempted for wavenumbers > 1600 cm^{-1}. Moreover, by considering amplitude differences between spectra as a function of wavelength, as in Figure 5, we can be more certain that any baseline offset between spectra does not influence our interpretation.

This finding has several implications for the wider interpretation of AFM-IR data. First, since the local reflectivity of the substrate clearly affects the magnitude of AFM-IR amplitude signals, features in the AFM-IR spectra and maps may correspond to any local heterogeneities of an underlying reflective substrate. This is particularly relevant for the analysis of industrial coatings, where factors affecting the local reflectivity of an underlying substrate may include local spots of adhesion loss, blistering, corrosion, or even the different
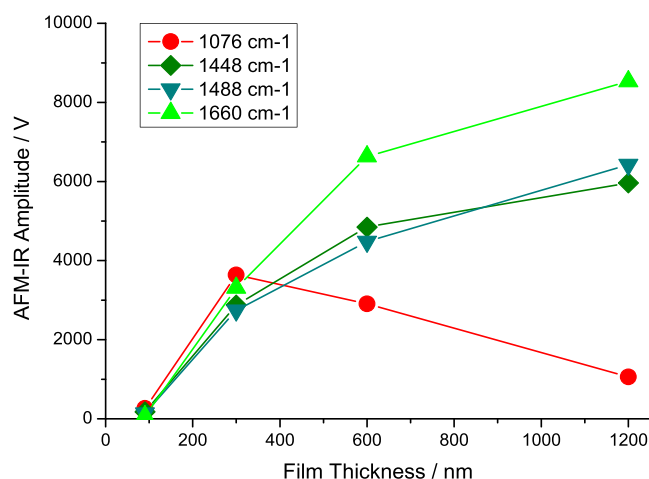
Figure 5. Difference between AFM-IR amplitude values obtained from the average of four individual spectra collected over gold decorated glass and glass only regions of the substrate at 1076, 1448, 1488, and 1600 cm^{-1}, as a function of the overlying polystyrene film thickness.
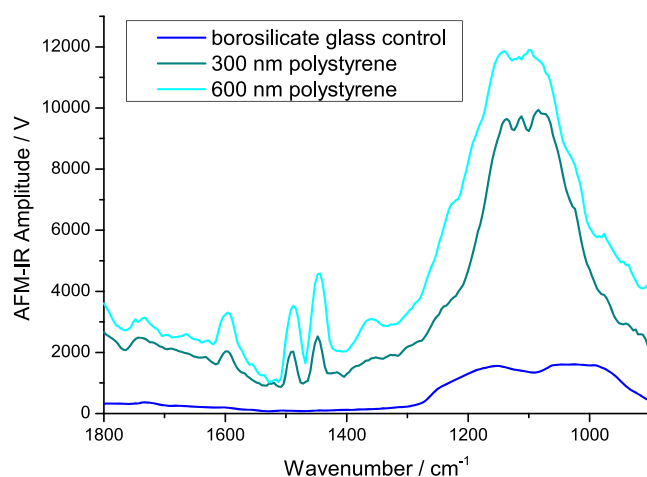

Figure 6. Average AFM-IR spectrum (of 20 individual measurements) gathered for an uncoated borosilicate glass substrate, and the average spectra (of 4 individual measurements) collected over borosilicate glass regions of a patterned substrate in the presence of 300 and 600 nm polystyrene coatings.

phases of alloys. On the other hand, in the case of good contact between thin organic specimens and homogeneously reflective sample supports (e.g., silicon wafer), the near-linear correlation found between the raw AFM-IR amplitude signal and film thickness (for submicron films) indicate that the approaches conventionally used to correct for variable sample topology, i.e., spectral normalization and ratio image generation, can be applied for data interpretation in the presence of reflectance.

The AFM-IR amplitude signal at 1076 cm^{-1} demonstrates that in some cases more detailed optical modeling is necessary, since the raw signal does not scale in the same manner with the film thickness, Figure 4. While signals at 1448, 1488, and 1600 cm^{-1} increase near-linearly over most of the polymer thickness range, the signal at 1076 cm^{-1} plateaus between 300 and 600 nm thickness. We propose two contributions to this different response: absorption from the glass substrate and thin-film interference effects.

Considering first absorption in the glass: since 1076 cm^{-1} corresponds to Si–O–Si bond vibrations, it is expected that a strong infrared absorption and heating will occur in the glass substrate (see Figure S4 for modeling of this absorption). However, it is not certain that this absorption would be detected by the AFM-IR at the surface, as the glass is both buried and will have a much lower coefficient of thermal expansion than the polymer. As discussed above, it is possible that this weak thermal response in the borosilicate glass substrate is amplified by thermal expansion of the overlying polystyrene film. To test this amplification hypothesis, control AFM-IR spectra of the uncoated borosilicate glass were performed. A weak band was indeed detected in the 1000–1200 cm^{-1} region, Figure 6, greatly amplified by the polymer overlayer. The magnitude of the glass absorption and thermal response is expected to vary only slightly with polystyrene film thickness (Figure S4), so although an initial amplification effect is seen between 90 and 300 nm, the contribution of glass expansion to the overall AFM-IR amplitude signal clearly diminishes as film thicknesses are further increased.

Considering thin-film interference effects, full optical modeling of IR absorption in the polymer at 1600 cm^{-1} (Figure S2) reveals that the first thin-film interference fringe at this wavelength occurs at a film thickness of approximately

1200 nm, with a strong signal enhancement over gold predicted for films of this thickness. Some evidence for this enhancement is seen in Figure 5, although the effect is likely suppressed by detection saturation as discussed above. In contrast, modeling at 1076 cm^{-1} reveals that the first thin-film interference fringe does not occur until approximately 1800 nm (Figure S3) with little interference-derived enhancement over gold for thinner films. This effect further serves to reduce the observed intensity difference between gold and glass at 1076 cm^{-1}. A full treatment of thin-film interference effects in AFM-IR will be presented in a subsequent manuscript.

Importantly, the more complex relationship to sample thickness observed at 1076 cm^{-1} negates the use of conventional AFM-IR morphology corrections (spectral normalization and ratio images) if the spectra and/or images are collected at wavelengths coincident with substrate absorption bands, even in cases where the underlying substrate is structurally homogeneous.

Given that reflectance of the infrared beam influences the photothermal AFM-IR amplitude signal, optical artifacts may be expected to occur.[54] These are well-known to arise in the experimentally similar RAIRS (reflectance-absorption infrared spectroscopy) technique due to the Fabry–Perot interference. During RAIRS of thin films, interference between infrared reflected at the surface of the sample and the emergent beam commonly imposes a periodic background fluctuation, which dominates thin film spectra. Our modeling (Figure S2 and Figure S3) has shown that for AFM-IR of the polystyrene films investigated, all film thicknesses encompass only the first interference fringe, giving only nonperiodic interference effects. In keeping with this, no tell-tale periodic patterns were observable in any of the AFM-IR spectra obtained over gold, Figure 2.

Evidence of interference effects can however be found when small fluctuations in the AFM-IR amplitude signal are directly visualized in AFM-IR amplitude maps. Local variations in interference may be expected, since the overall intensity of radiation reaching the polymer in contact with the probe will vary according to the tip (and therefore incident beam) position, as illustrated in Scheme 2. (For simplicity, Scheme 2 shows only light reflected by the gold, whereas, in reality,

Scheme 2. Illustration of Multiple Infrared Reflections over Gold Decorated Regions of the Substrate, Where Interference between the Two Reflected Beams May Occur (Left), and Single Reflectance from the Gold Region, Where No Interference Occurs for the Reflected Radiation (Right)
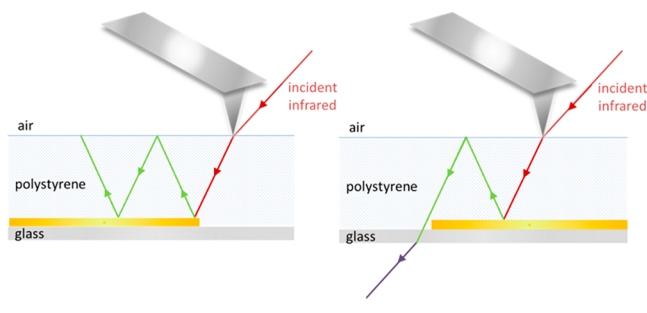
weaker reflection, and rereflection, will also occur over glass regions, see Figure S1). For thicker films, a "shadow" effect was seen in images, overlaid on the bright squares corresponding to reflection from the gold regions, Figure 7. These shadows are attributed to destructive interference for 1150 and 3000 nm thick films imaged at 2848 cm^{-1}. Supporting evidence that these shadow features correspond to optical interference was found in the wavelength dependence of the contrast. For the 3000 nm thick film, constructive interference yielded locally brighter contrast when mapped using 1600 cm^{-1} illumination, in the same region as destructive interference generated shadow effects in maps obtained at 2848 and 2920 cm^{-1}, Figure 8.

Furthermore, the displacement between an interference effect (a shadow in the case of destructive interference) and the edge of the bright square will be dictated by the refraction of infrared light inside the polymer film and the film thickness. This was found to be the case; the distance between the apparent edge of the gold square and the edge of the shadows in the images shown in Figure 7 scaled approximately with film thickness. These were measured to be 8 and 18 μm for the polystyrene layers of 1150 and 3000 nm thickness.

It is nonetheless necessary to consider a feasible alternative explanation for these shadow effects: uneven heating of the specimen as a result of contrasting reflectivity across the patterned substrates. This is expected to cause the overall sample surface to heat up in many places, creating a photothermal oscillation of the air above the sample. A control experiment was devised to test if this was the case; after imaging a region of a 3000 nm thick coating with clear shadow effects, the AFM tip was withdrawn by progressively lowering the set point until contact was lost (signified by no response in the height scan), Figure 9. Scanning under otherwise identical conditions then demonstrated that the AFM probe indeed
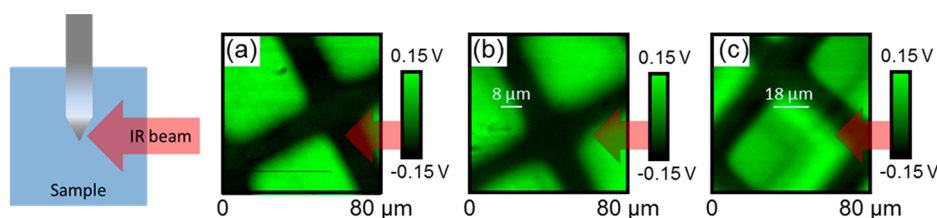

Figure 8. AFM-IR infrared induced amplitude maps of 3000 nm thick polystyrene films deposited onto gold-decorated borosilicate glass substrates. Images were obtained using incident infrared at (a) 1600, (b) 2848, and (c) 2920 cm^{-1}. Red arrows illustrate the direction of infrared illumination.
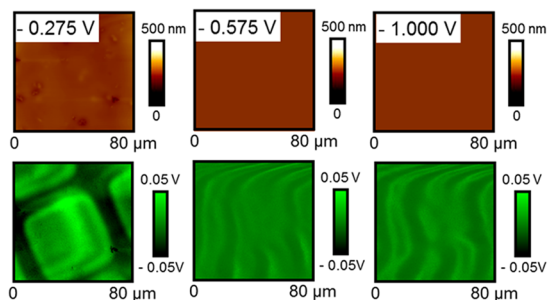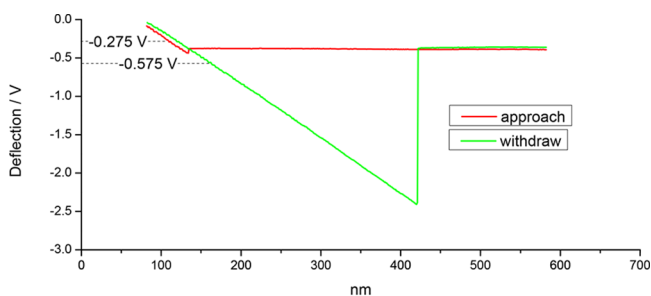
Figure 9. (Top) AFM probe deflection as a function of tip−sample separation for a 3000 nm thick polystyrene film deposited onto a gold-decorated borosilicate glass substrate, and (bottom) AFM-IR height and IR-amplitude images obtained using incident infrared at 1600 cm^{-1} with deflection set points at (a) −0.275, (b) −0.575 V, and (c) −1.000 V.

responds to photothermal oscillation of the air just above the sample. However, the AFM-IR amplitude maps obtained in this manner show that the portion of signal due to this effect does not correspond to the shadow effects observed in contact mode AFM-IR maps.

■ CONCLUSIONS

Reflection from the underlying substrate produces distinctive, wavelength-dependent features in local infrared spectra obtained using AFM-IR. Uniquely, this means that by using

Figure 7. Top-down view of the AFM-IR setup, showing the orientation of the probe and the direction of IR illumination and AFM-IR infrared induced amplitude maps gathered using incident excitation at 2848 cm^{-1} for polystyrene films deposited onto gold decorated borosilicate glass substrates. Film thicknesses were (a) 600, (b) 1150, and (c) 3000 nm. Red arrows illustrate the direction of infrared illumination.
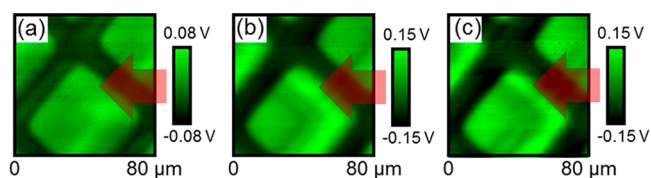
AFM-IR, information relating to the local composition of a buried substrate may be obtained in a nondestructive manner, alongside chemical analysis of an overlying film. This raises the intriguing possibility of expanding the photothermal infrared approach to include the indirect detection of discontinuities of metallic substrates. Nonetheless, for AFM-IR analysis of thin films, these results clearly indicate that the specular reflectance of an underlying substrate, its thermal response, and weak interference effects have a bearing on local spectra and infrared maps. The nature of the underlying substrate and local variations in specimen thickness should therefore be carefully considered when interpreting AFM-IR data.

■ ASSOCIATED CONTENT

ⓢ Supporting Information

The Supporting Information is available free of charge at https://pubs.acs.org/doi/10.1021/acs.analchem.9b05793.

> Calculations of interface reflectivities using CompleteEase ellipsometry software, and full modeling of the absorbed intensity for polystyrene film on gold-decorated glass or glass alone using RefFIT (PDF)

■ AUTHOR INFORMATION

Corresponding Author

Suzanne Morsch − *School of Materials, The University of Manchester, Manchester M13 9PL, United Kingdom;* ⓞ orcid.org/0000-0003-3883-2710; Phone: +44 161 306 2914; Email: Suzanne.morsch@manchester.ac.uk

Authors

Stuart Lyon − *School of Materials, The University of Manchester, Manchester M13 9PL, United Kingdom*

Steve Edmondson − *School of Materials, The University of Manchester, Manchester M13 9PL, United Kingdom;* ⓞ orcid.org/0000-0001-9036-7559

Simon Gibbon − *AkzoNobel, Stoneygate Lane, Felling, Gateshead, Tyne and Wear NE10 0JY, United Kingdom;* ⓞ orcid.org/0000-0002-8312-8602

Complete contact information is available at:
https://pubs.acs.org/10.1021/acs.analchem.9b05793

Notes

The authors declare no competing financial interest.

■ ACKNOWLEDGMENTS

■ REFERENCES

(1) Xiao, L.; Schultz, Z. D. *Anal. Chem.* **2018**, *90*, 440−458.

(2) Fu, W.; Zhang, W. *Small* **2017**, *13*, 1603525.

(3) Schmid, T.; Opilik, L.; Blum, C.; Zenobi, R. *Angew. Chem., Int. Ed.* **2013**, *52*, 5940−5954.

(4) Keilmann, F.; Hillenbrand, R. *Philos. Trans. R. Soc., A* **2004**, *362*, 787−805.

(5) Dazzi, A.; Prater, C.; Hu, Q.; Chase, D. B.; Rabolt, J. F.; Marcott, C. *Appl. Spectrosc.* **2012**, *66*, 1365−1384.

(6) Dazzi, A.; Prater, C. B. *Chem. Rev.* **2017**, *117*, 5146−5173.

(7) Nguyen, T. V.; Le, X. H.; Dao, P. H.; Decker, C.; Nguyen-Tri, P. *Prog. Org. Coat.* **2018**, *124*, 137−146.

(8) Morsch, S.; Lyon, S.; Gibbon, S. R. *Prog. Org. Coat.* **2017**, *102*, 37−43.

(9) Nguyen-Tri, P.; Prud'homme, R. E. *J. Photochem. Photobiol., A* **2019**, *371*, 196−204.

(10) Morsch, S.; Van Driel, B. A.; Van Den Berg, K. J.; Dik, J. *ACS Appl. Mater. Interfaces* **2017**, *9*, 10169−10179.

(11) Morsch, S.; Bastidas, P. D.; Rowland, S. M. *J. Mater. Chem. A* **2017**, *5*, 24508−24517.

(12) Fini, E. H.; Hung, A. M.; Roy, A. *ACS Sustainable Chem. Eng.* **2019**, *7*, 10340−10348.

(13) Yang, J.; Hatcherian, J.; Hackley, P. C.; Pomerantz, A. E. *Nat. Commun.* **2017**, *8*, 2179.

(14) Hassenkam, T.; Andersson, M. P.; Dalby, K. N.; Mackenzie, D. M. A.; Rosing, M. T. *Nature* **2017**, *548*, 78−81.

(15) Imbert, L.; Gourion-Arsiquaud, S.; Villarreal-Ramirez, E.; Spevak, L.; Taleb, H.; van der Meulen, M. C. H.; Mendelsohn, R.; Boskey, A. L. *PLoS One* **2018**, *13*, No. e0202833.

(16) Sereda, G.; VanLaecken, A.; Turner, J. A. *Dent. Mater.* **2019**, *35*, 617−626.

(17) Morsch, S.; Emad, S.; Farren, L. A.; Goodall, M. D.; Lyon, S. B.; Gibbon, S. R. *Sci. Rep.* **2018**, *8*, 17450.

(18) Weiss, V. U.; Wieland, K.; Schwaighofer, A.; Lendl, B.; Allmaier, G. *Anal. Chem.* **2019**, *91*, 3860−3868.

(19) Bondy, A. L.; Kirpes, R. M.; Merzel, R. L.; Pratt, K. A.; Banaszak Holl, M. M.; Ault, A. P. *Anal. Chem.* **2017**, *89*, 8594−8598.

(20) Rickard, M. A.; Meyers, G. F.; Habersberger, B. M.; Reinhardt, C. W.; Stanley, J. J. *Polymer* **2017**, *129*, 247−251.

(21) Tri, P. N.; Prud'Homme, R. E. *Macromolecules* **2018**, *51*, 181−188.

(22) Tai, T.; Karácsony, O.; Bocharova, V.; Van Berkel, G. J.; Kertesz, V. *Anal. Chem.* **2016**, *88*, 2864−2870.

(23) Nguyen Tri, P.; Prud'Homme, R. E. *Macromolecules* **2018**, *51*, 7266−7273.

(24) Morsch, S.; Liu, Y.; Lyon, S. B.; Gibbon, S. R. *ACS Appl. Mater. Interfaces* **2016**, *8*, 959−966.

(25) Morsch, S.; Liu, Y.; Greensmith, P.; Lyon, S. B.; Gibbon, S. R. *Polymer* **2017**, *108*, 146−153.

(26) Morsch, S.; Kefallinou, Z.; Liu, Y.; Lyon, S. B.; Gibbon, S. R. *Polymer* **2018**, *143*, 10−18.

(27) Mikhalchan, A.; Banas, A. M.; Banas, K.; Borkowska, A. M.; Nowakowski, M.; Breese, M. B. H.; Kwiatek, W. M.; Paluszkiewicz, C.; Tay, T. E. *Chem. Mater.* **2018**, *30*, 1856−1864.

(28) Rosenberger, M. R.; Wang, M. C.; Xie, X.; Rogers, J. A.; Nam, S.; King, W. P. *Nanotechnology* **2017**, *28*, 355707.

(29) Bartlam, C.; Morsch, S.; Heard, K. W. J.; Quayle, P.; Yeates, S. G.; Vijayaraghavan, A. *Carbon* **2018**, *139*, 317−324.

(30) Ruggeri, F. S.; Longo, G.; Faggiano, S.; Lipiec, E.; Pastore, A.; Dietler, G. *Nat. Commun.* **2015**, *6*, 7831.

(31) Ruggeri, F. S.; Vieweg, S.; Cendrowska, U.; Longo, G.; Chiki, A.; Lashuel, H. A.; Dietler, G. *Sci. Rep.* **2016**, *6*, 31155.

(32) Perez-Guaita, D.; Kochan, K.; Batty, M.; Doerig, C.; Garcia-Bustos, J.; Espinoza, S.; McNaughton, D.; Heraud, P.; Wood, B. R. *Anal. Chem.* **2018**, *90*, 3140−3148.

(33) Farber, C.; Wang, R.; Chemelewski, R.; Mullet, J.; Kurouski, D. *Anal. Chem.* **2019**, *91*, 2472−2479.

(34) Hill, G. A.; Rice, J. H.; Meech, S. R.; Craig, D. Q. M.; Kuo, P.; Vodopyanov, K.; Reading, M. *Opt. Lett.* **2009**, *34*, 431−433.

(35) Dazzi, A.; Prazeres, R.; Glotin, F.; Ortega, J. M. *Ultramicroscopy* **2007**, *107*, 1194−1200.

(36) Policar, C.; Waern, J. B.; Plamont, M.-A.; Clède, S.; Mayet, C.; Prazeres, R.; Ortega, J.-M.; Vessières, A.; Dazzi, A. *Angew. Chem., Int. Ed.* **2011**, *50*, 860−864.

(37) Wang, Y.; Heinemann, F.; Top, S.; Dazzi, A.; Policar, C.; Henry, L.; Lambert, F.; Jaouen, G.; Salmain, M.; Vessieres, A. *Dalton Trans.* **2018**, *47*, 9824−9833.

(38) Deniset-Besseau, A.; Prater, C. B.; Virolle, M.-J.; Dazzi, A. *J. Phys. Chem. Lett.* **2014**, *5*, 654−658.

(39) Ramer, G.; Aksyuk, V. A.; Centrone, A. *Anal. Chem.* **2017**, *89*, 13524−13531.

(40) Lahiri, B.; Holland, G.; Centrone, A. *Small* **2013**, *9*, 439−445.

(41) Waeytens, J.; Doneux, T.; Napolitano, S. *ACS Appl. Polym. Mater.* **2019**, *1*, 3−7.

(42) Morsch, S.; Lyon, S.; Greensmith, P.; Smith, S. D.; Gibbon, S. R. *Faraday Discuss.* **2015**, *180*, 527−542.

(43) Morsch, S.; Liu, Y.; Malanin, M.; Formanek, P.; Eichhorn, K.-J. *ACS Appl. Nano Mater.* **2019**, *2*, 2494−2502.

(44) Tang, F.; Bao, P.; Su, Z. *Anal. Chem.* **2016**, *88*, 4926−4930.

(45) Dazzi, A.; Glotin, F.; Carminati, R. *J. Appl. Phys.* **2010**, *107*, 124519.

(46) Kjoller, K.; Felts, J. R.; Cook, D.; Prater, C. B.; King, W. P. *Nanotechnology* **2010**, *21*, 185705.

(47) Mayet, C.; Dazzi, A.; Prazeres, R.; Ortega, J.-M.; Jaillard, D. *Analyst* **2010**, *135*, 2540−2545.

(48) Jitian, S. Determination of Optical Constants of Polystyrene Films from IR Reflection-Absorption Spectra. In *Processes in Isotopes and Molecules*. AIP Conference Procedings, Cluj Napoca, Romania, Sept 29−Oct 1, 2011; AIP, 2012; Vol. *18*, pp 41−48,.

(49) Amma, S. I.; Luo, J.; Pantano, C. G.; Kim, S. H. *J. Non-Cryst. Solids* **2015**, *428*, 189−196.

(50) Luo, J.; Smith, N. J.; Pantano, C. G.; Kim, S. H. *J. Non-Cryst. Solids* **2018**, *494*, 94−103.

(51) Kitamura, R.; Pilon, L.; Jonasz, M. *Appl. Opt.* **2007**, *46*, 8118−8133.

(52) Rosenberger, M. R.; Wang, M. C.; Xie, X.; Rogers, J. A.; Nam, S.; King, W. P. *Nanotechnology* **2017**, *28*, 355707.

(53) Rice, J. H.; Hill, G. A.; Meech, S. R.; Kuo, P.; Vodopyanov, K.; Reading, M. *Eur. Phys. J.: Appl. Phys.* **2010**, *51*, 21202.

(54) Mayerhöfer, T. G.; Pahlow, S.; Hübner, U.; Popp, J. *Analyst* **2018**, *143*, 3164−3175.